




Research Article

Zn_{1-x}Fe_xO_y nanocomposites for renewable hydrogen produced efficiently via photoelectrochemical *vis-a-vis* photocatalytic splitting of water

Nirupama Singh¹ · Mrinal R. Pai³ · Gurpreet Kaur¹ · Divya¹ · Vibha R. Satsangi² · Sahab Dass¹ · Rohit Shrivastav¹ 

© Springer Nature Switzerland AG 2019

Abstract

Zn_{1-x}Fe_xO_y nanocomposites have been investigated for bi-functional performance towards photoelectrochemical (PEC) and photocatalytic (PC) splitting of water to produce hydrogen. Prepared at varying Zn/Fe atomic ratio via co-precipitation through controlled addition of NH₄OH to the aqueous solution of iron (III) nitrate nonahydrate [Fe(NO₃)₃·9H₂O] and zinc acetate dihydrate [(CH₃COO)₂Zn·2H₂O], followed by sintering in air at 800 °C, the nanocomposites were characterized by XRD, SEM, TEM, UV-Visible optical absorption, XPS, and Mössbauer spectral analysis. Shift in bandgap energy (E_g) and alterations in microstructural characteristics and electrical properties, observed with change in sample-composition, significantly influenced hydrogen generation. Plausible reasons have been offered. The optimum conditions for hydrogen generation via PEC and PC routes, not being similar, have also been worked out.

Keywords Photocatalytic · Photoelectrochemical · Water splitting · Hydrogen · Nanocomposites · ZnO · Fe₂O₃

1 Introduction

Most enduring solution to the world's burgeoning energy needs probably lies in switching over from fossil-fuel-dependent society to solar-hydrogen era. Hence, studies pertaining to the development of commercially-viable methods for hydrogen generation by solar splitting of water have drawn huge interest in recent years [1–4]. Photoelectrochemical (PEC) and photocatalytic (PC) splitting of water are important in the above context, especially due to ease of operation, low-cost, and expected high efficiency of energy conversion. The PC process involves the use of a photocatalyst (usually semiconductor), capable to generate required thermodynamic yield of hydrogen via splitting of water [3]. In PEC process the semiconductor is used as photoelectrode and it must possess appropriate optical, electrical, and electronic properties to facilitate harvest of photons and migration of photogenerated

charge carriers in electrochemical reaction pathway [4]. The three essential steps in photo-splitting of water are: (1) absorption of light ($h\nu \geq$ band gap) by semiconductor, (2) production and separation of charge carriers, and (3) occurrence of redox reactions leading to splitting of water [5]. Since, it is the visible part in the solar spectrum that carries maximum energy from Sun to the Earth's surface; the development of visible-light-driven photocatalyst/photoelectrode is of paramount importance to realise the ultimate goal of efficient conversion of solar energy to hydrogen.

Ever since the first report on UV light-induced splitting of water on TiO₂ photanode [6], a whole range of semiconductors has been investigated for this application. Besides, several approaches have been tried to optimise the optical bandgap, electrical and electronic properties of the semiconductor with regard to the splitting of water [7, 8]. Researches pertaining to the use of layered/mixed

✉ Rohit Shrivastav, rohitshrivastav_dei@yahoo.co.in | ¹Department of Chemistry, Dayalbagh Educational Institute, Dayalbagh, Agra 282 005, India. ²Department of Physics and Computer Science, Dayalbagh Educational Institute, Dayalbagh, Agra 282 005, India. ³Chemistry Division, Bhabha Atomic Research Centre, Mumbai 400 085, India.



SN Applied Sciences (2019) 1:611 | <https://doi.org/10.1007/s42452-019-0597-y>

Received: 18 October 2018 / Accepted: 10 May 2019 / Published online: 20 May 2019

semiconductors, swift heavy ion irradiation and surface modifications have been pursued with lot of optimism in recent years [9–11]. Plasmon mediated and fullerene modified materials have also yielded much improvement in visible light induced photocatalytic hydrogen generation [12–15]. The advent of nanomaterials and nanotechnology has generated a renewed interest in this area. In few reports, nanomaterials have shown much improved PEC/PC performance against their bulk counterparts for photosplitting of water [16, 17].

Discovery of new and improvement in the known semiconductors, capable to split water efficiently under solar illumination, forms the core of research in this area [18–20]. As a primary requirement the semiconductor photocatalyst/photoelectrode must be chemically stable with an optimum band gap ~ 1.8 to 2.2 eV, in order to efficiently absorb bulk of solar radiations [21, 22]. Semiconductors, such as TiO_2 [23, 24], SrTiO_3 [25], SnO_2 [26] and BaTiO_3 [27] with relatively high band gap cannot absorb large portion of visible light. On the other hand, low band gap materials, viz, Si [28], GaAs [29] and InP [30] are generally unstable and suffer corrosion in contact with the electrolyte. ZnO and $\alpha\text{-Fe}_2\text{O}_3$, the key technological materials [31], have been explored earlier for PEC/PC splitting of water [32, 33]. While $\alpha\text{-Fe}_2\text{O}_3$ has an optimum band gap of 2.2 eV, ZnO is relatively a high band gap material. The conduction and valence band edges of ZnO straddle perfectly $\text{H}_2\text{O}/\text{H}_2$ and OH^-/O_2 redox levels, thereby satisfying a mandatory requirement for spontaneous photosplitting of water. But, band edges in $\alpha\text{-Fe}_2\text{O}_3$ are not well aligned and external bias is needed in this case to thrust the charge carriers for redox reactions. Further, electron mobility in ZnO is high and in fact even higher than TiO_2 . In contrast, $\alpha\text{-Fe}_2\text{O}_3$ is known to be a material with high electrical resistance due to thermally controlled hopping mechanism for charge carrier mobility [34]. The ZnO- $\alpha\text{-Fe}_2\text{O}_3$ combination can, thus, be an interesting system for PEC/PC applications.

In continuation to our earlier works on the PEC and PC splitting of water using doped/undoped nanostructured oxide semiconductors [35–37], here we have attempted to overcome the limitation of high band gap of ZnO by evolving $\text{Zn}_{1-x}\text{Fe}_x\text{O}_y$ nanocomposites (prepared in powder form at varying Zn/Fe atomic ratio). The variation in PEC/PC performance of samples was analysed by observed changes in crystal, microstructural, optical and electrical properties. Despite, the basic mechanism of photoexcitation, charge carrier generation and transport being same in both the PC and PEC splitting of water; the two processes are probably differently controlled by some still ambiguous parameters/semiconductor characteristics. In most previous studies researchers worked either on PEC or PC splitting of water. Working with the same set of materials, this study is also an attempt to evolve a comparison

between PEC and PC splitting of water with regard to the properties of the semiconductor used.

2 Experimental

2.1 Preparation of $\text{Zn}_{1-x}\text{Fe}_x\text{O}_y$ nanocomposites

To the aqueous solution of iron (III) nitrate nonahydrate [$\text{Fe}(\text{NO}_3)_3 \cdot 9\text{H}_2\text{O}$] and zinc acetate dihydrate [$(\text{CH}_3\text{-COO})_2\text{Zn} \cdot 2\text{H}_2\text{O}$], controlled addition ($1 \text{ cm}^3 \text{ min}^{-1}$) of ammonium hydroxide solution under continuous stirring till the pH ascended to ≈ 7 enabled co-precipitation [38]. The precipitate was washed using ethyl alcohol, allowed to age for 24 h, and dried for 1 h at 80°C . To complete the cycle of crystallization, samples were sintered in air in three stages as: Stage I \rightarrow 30 min at 250°C , Stage II \rightarrow 30 min at 600°C , and Stage III \rightarrow 60 min at 800°C . Step sintering with intermittent grinding was attempted to avoid heat-shock and also to ensure the completion of reaction and chemical/structural uniformity in samples prepared.

2.2 Characterization

Samples were subjected to XRD analysis using glancing angle X-ray diffractometer (Bruker AXS D8 Advance, Germany), equipped with graphite monochromator, a mirror at a fixed incidence angle of $1^\circ\text{--}5^\circ$ and $\text{CuK}\alpha$ as the radiation source. The angular accuracy was 0.001° and the angular resolution was better than 0.01° . The analysis was made at 2θ varying from 25° to 60° with a step size of 0.02 degrees min^{-1} . Average crystallite size in samples was estimated by Scherrer's computations utilizing the XRD data and Eq. 1 [35–37],

$$p = k\lambda / B \cos\theta, \quad (1)$$

where p is average crystallite size, B the full width at half maximum, λ the wavelength of X-ray (1.542 \AA), and θ the half diffraction angle of the centroid. The observed XRD data was further utilized to estimate the dislocation density (δ) and microstrain (ϵ) in the samples [39] by employing Eqs. 2 and 3,

$$\delta = 1/t^2 \quad (2)$$

$$\epsilon = B \cos\theta / 4 \quad (3)$$

The optical characteristics of samples were investigated using diffuse reflectance UV-Vis spectrophotometer (Perkin Elmer, Lambda 650S) in the range $200\text{--}800 \text{ nm}$. Pure BaSO_4 was used as reflectance standard. The absorbance data was utilized to evaluate optical band gap energy (E_g) of the samples [37].

Surface morphology of samples was investigated by recording SEM images using Scanning Electron Microscope (Tescan Vega MV 2300T/40, 25 kV accelerating voltage, ~ 10 mm working distance). Considering the dimensions of 80–100 randomly chosen particles in the SEM images and using J-image software, a tentative pattern of particle size distribution in the samples was obtained.

Mössbauer spectrometer (Nucleonix Systems Pvt. Ltd., Hyderabad, India), operated in constant acceleration mode (triangular wave) in transmission geometry, was used to record Mössbauer spectrum of samples at room temperature (27 ± 3 °C). The Co-57 in Rh matrix of strength 50 mCi was used as source. The isomer shifts were recorded relative to α -57 Fe metal foil, which was also used for velocity scale calibration with the effective nuclear hyperfine field H_{eff} 331 k Oe. The outer line width of calibration spectra was 0.29 mm s^{-1} .

The sample ZnFe(70) was treated as a representative case for XPS analysis to investigate the oxidation state of different elements. The analysis was made on SPEC high resolution spectrometer (Surface Nano Analysis GmbH), using Mg-K α radiation. This sample was also subjected to TEM analysis to obtain a closer view on the morphology of particles. FEI Technai G² 20 system was employed at 200 kV accelerating voltage to record images.

2.3 PEC study

For PEC studies, sample disks (diameter 1 cm, thickness 1 mm) were generated by pressing 1 g of powder sample in KBr press (Techno Search Instruments, Mumbai) at pressure 7 tones cm^{-2} . The disks were re-sintered at 600 °C for 1 h to provide mechanical strength and subsequently used as working electrode (WE) in PEC cell. Ohmic electrical contact was created from one surface of the disk using silver paint and copper wire. Leaving open 1 cm^2 area at the centre of the other side of the disk for illumination, the electrical contact and the side edges of the disk were perfectly sealed by non-transparent, non-conducting epoxy resin (Hysol; Dexter, Singapore). PEC studies were conducted in three electrode configuration electrochemical cell, comprising platinum mesh auxiliary electrode (AE) and saturated calomel reference electrode (SCE). The PEC cell, filled with aqueous solution of NaOH (0.01 M, pH 12, used as electrolyte), was surrounded by a water jacket to avert infrared radiations heat effect. Potentiostat (Model ECDA-001, Conserv Enterprises) and 150 W Xenon Arc light source (Ozone-free; Oriel, USA) were employed to obtain current–voltage (J–V) characteristic plots under darkness and illumination. Observed photocurrent values were used to determine the Applied Bias Photon-to-Current Efficiency (ABPE), defined by the following equation [40].

$$ABPE = \left[\frac{J_{ph} (\text{mAcm}^{-2}) \times (1.23 - |V|)(V)}{P_{total} (\text{mWcm}^{-2})} \right] \quad (4)$$

where J_{ph} is the photocurrent density obtained under applied bias (V_b) and P_{total} is incident illumination power density in mW cm^{-2} .

2.4 PC study

The photocatalytic activity of the samples was estimated in batches in a closed rectangular quartz cell photoreactor (PR), equipped with sampling and evacuation ports. A medium-pressure mercury lamp (LS) (Hg, Ace Glass Inc., 450 W), with broad range emission (16% in UV and 84% in visible region), was used as light source. LS was surrounded with external water jacket to prevent heat effect of IR radiations. Weighed amount (0.1 g) of powder sample was loaded as dispersion in the PR filled with methanol and water (total volume 15 cm^3 , in the ratio 1:2 V/V). De-aerated PR was irradiated for intervals of 2, 4, 6 and 8 h and hydrogen evolution was estimated quantitatively by Gas Chromatograph (Netel Michro-1100), equipped with TC detector, Molecular Sieve and Ar carrier gas. Apparent Quantum Efficiency (AQE) of different photocatalysts was estimated according to Refs. [37, 40].

In the study, chemicals with purity > 99.9%, and double distilled deionized water (specific conductance < $10^{-6} \text{ mho cm}^{-1}$) were used. Triplicate-quadruplicate measurements yielded results within $\pm 15.2\%$ deviations.

3 Results and discussion

3.1 Microstructural characteristics: XRD analysis

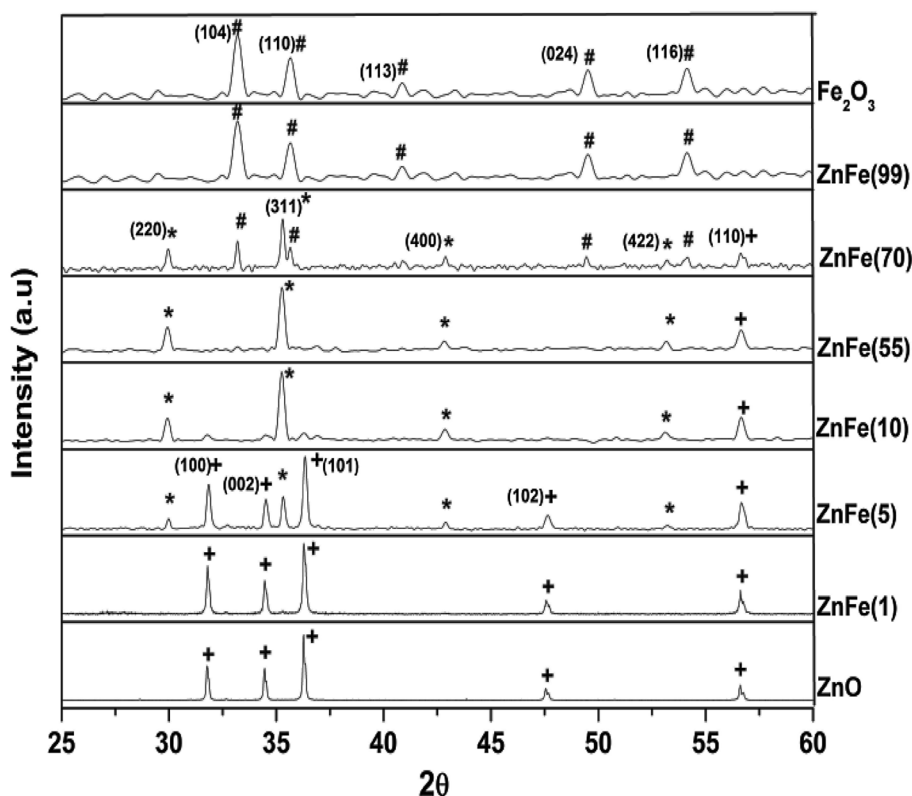
The colour of samples changed gradually from white to brick red with increase in Fe content. Table 1, lists the crystal phase/s identified and lattice parameters evaluated in samples from XRD analysis. The XRD patterns (Fig. 1) of samples ZnO and ZnFe(1), show intense peaks at $2\theta = 31.7^\circ, 34.4^\circ, 36.2^\circ, 47.6^\circ$ and 56.6° which correspond to (100), (002), (101), (102) and (110) planes, respectively, of hexagonal wurtzite phase of ZnO (JCPDS, Card 89-0510). In sample ZnFe(5), presence of secondary phase (ZnFe₂O₄ spinel) is evident by observed XRD reflections at $2\theta = 29.9^\circ, 35.3^\circ, 42.8^\circ, 53.1^\circ$ and 56.7° corresponding to planes (220), (311), (400), (422) and (511), respectively (JCPDS, Card 22-1012). However, the possibility of the peak at $2\theta 56.7^\circ$ getting overlapped with a possible peak at 56.6° corresponding to wurtzite ZnO cannot be totally ruled out. The

Table 1 Nominal composition and identified crystal phases in samples

Metal concentration (at.%)		Nominal composition (Zn _{1-x} Fe _x O _y)	Phases identified by XRD	Lattice parameters (Å)	Sample abbreviate
Zn	Fe				
100	–	ZnO	ZnO	a=3.248, c=5.205	ZnO
99	1	Zn _{0.99} Fe _{0.01} O _y	ZnO	a=3.248, c=5.205	ZnFe(1)
95	5	Zn _{0.95} Fe _{0.05} O _y	ZnO	a=3.248, c=5.205	ZnFe(5)
90	10	Zn _{0.90} Fe _{0.10} O _y	ZnFe ₂ O ₄	a=b=c=8.441	ZnFe(10)
45	55	Zn _{0.45} Fe _{0.55} O _y	ZnFe ₂ O ₄	a=b=c=8.441	ZnFe(55)
30	70	Zn _{0.30} Fe _{0.70} O _y	ZnFe ₂ O ₄	a=b=c=8.441	ZnFe(70)
1	99	Zn _{0.01} Fe _{0.99} O _y	Fe ₂ O ₃	a=5.032, c=13.733	ZnFe(99)
–	100	Fe ₂ O ₃	Fe ₂ O ₃	a=5.032, c=13.733	Fe ₂ O ₃

y, undefined

Fig. 1 XRD pattern of samples. Peaks correspond to: *Wurtzite ZnO, #α-Fe₂O₃, and *ZnFe₂O₄



samples ZnFe(10) and ZnFe(55) were observed to be single-phasic with the existence of ZnFe₂O₄ spinel phase. Formation of cubic structured nanoparticles of XY₂O₄ (X and Y represented by bivalent and trivalent metal, respectively) has been reported earlier also and are shown to exhibit high chemical stability [41–43]. Further, in sample ZnFe(70) the emergence of rhombohedral hematite phase (α-Fe₂O₃) is observed with the reflections at 33.1°, 35.6°, 40.8°, 49.5° and 54.1° from (104), (110), (113), (024) and (116) planes,

respectively (JCPDS, Card 89-0599). In samples ZnFe(99) and Fe₂O₃, single-phase existence of hematite occurred. It can also be conjectured that the single-phase metal oxide phases (wurtzite ZnO and α-Fe₂O₃) observed in samples ZnFe(1), ZnFe(5) and ZnFe(99) are in fact doped oxides having dopant metal ion concentration less than 5%. Above contention is supported from the observed shift in the XRD peaks, which is probably indicative of strain building-up in the lattice due to size difference in the two

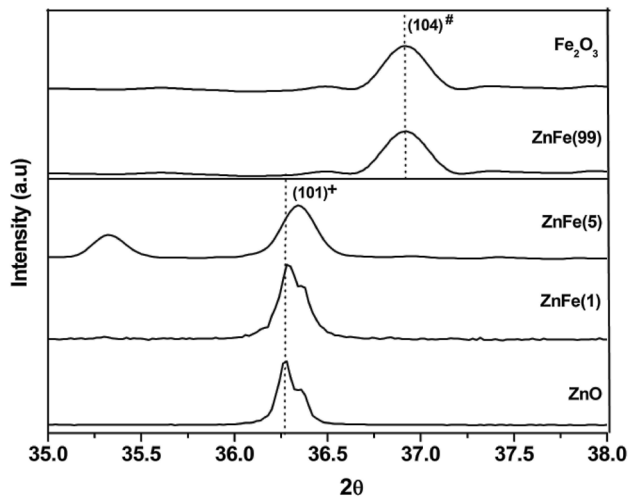


Fig. 2 Observed peak shift in XRD pattern of samples. Peaks correspond to: Wurtzite ZnO (⁺), α -Fe₂O₃ ([#])

cations (Fig. 2). The average crystallite size ranged from 42 to 68 nm (Table 2). The presence of dopant cation seems to impart a diminishing effect to the growth of an oxide phase leading to decrease in crystallite size. The effect is also evident from the increase in dislocation density and microstrain (Table 2) at comparable concentrations of the two cations. At the extreme ends of concentration variation, dislocation density and microstrain increases and average crystallite size decreases.

3.2 Morphology

SEM images of samples are shown in Fig. 3. The wurtzite phase of ZnO is marked by presence of hexagonal shaped particles. As the Fe concentration increases the dominance of spherical particles increases. The Fe incorporation in samples seems to decrease the grain agglomeration. At comparable concentrations of Zn and Fe, the clearly visible lesser spherical structures may be attributed to the existence of ZnFe₂O₄ cubic spinel phase (as observed in XRD

analysis). Particle features are not clear in samples lying at extreme ends of concentration variation [44]. The particle size distribution (Fig. 4) revealed average particle size in the range 100–220 nm which is ~ 2 to 4 times higher compared to the estimations from Scherrer's computations based on XRD data. The discrepancy in the values suggests significant grain agglomeration in samples, with particles seen in SEM images indeed being grain agglomerates.

In the observed TEM image (Fig. 5) of sample ZnFe(70), by analysing different regions and particle interfaces, not only the lattice fringes appear continuous, but the presence of both ZnO and α -Fe₂O₃ is also indicated. As estimated from fringe width, the distances between adjacent crystal planes are 0.36 nm for (104) plane of α -Fe₂O₃ and 0.26 nm for (101) plane of ZnO. Above observation suggests that the simultaneous occurrence of ZnO and α -Fe₂O₃ in samples cannot be totally ruled out, although the XRD analysis has very clearly indicated the emergence of doped structures of single phase oxides at extreme ends and the secondary phase of ZnFe₂O₄ in the middle region of composition-variation.

3.3 Optical characteristics

Apparently guided by variations in crystallinity and stoichiometry, the DRUV-Vis absorption spectra of samples (Fig. 6) indicate a significant shift in absorption edge to higher wavelengths, on increasing Fe/Zn concentration ratio. In samples with dominant growth of ZnO, sharp absorption edge in the UV region (~ 400 nm), a characteristic of hexagonal wurtzite phase of ZnO, indicate the onset of fundamental absorption corresponding to O:2p → Zn:4s charge-transfer band. The estimated values of band gap energy (E_g) of samples are presented in Fig. 7, which shows that with Fe/Zn concentration ratio increasing from 0.43 to 4.00, E_g decreases from 3.2 to 1.8 eV, almost linearly with increase in Fe concentration.

Table 2 Estimated values of average crystallite size (p), dislocation density (δ), microstrain (ϵ), electrical resistivity (r) and band gap energy (E_g)

Sample abbreviate	Nominal composition (Zn _{1-x} Fe _x O _y)	p (nm)	$\delta \times 10^{-14}$ (line ² m ⁻²)	$\epsilon \times 10^{-3}$	r (k Ω cm)	E_g (eV)
ZnO	ZnO	60	2.7	5.7	2.89	3.14
ZnFe(1)	Zn _{0.99} Fe _{0.01} O _y	51	3.8	6.7	2.77	3.01
ZnFe(5)	Zn _{0.95} Fe _{0.05} O _y	52	3.6	6.6	4.31	3.08
ZnFe(10)	Zn _{0.90} Fe _{0.10} O _y	49	4.1	6.9	5.35	2.93
ZnFe(55)	Zn _{0.45} Fe _{0.55} O _y	42	5.6	8.3	7.55	2.51
ZnFe(70)	Zn _{0.30} Fe _{0.70} O _y	49	4.1	6.9	7.78	1.80
ZnFe(99)	Zn _{0.01} Fe _{0.99} O _y	60	2.7	5.8	8.51	1.88
Fe ₂ O ₃	Fe ₂ O ₃	68	2.1	5.0	8.60	1.92

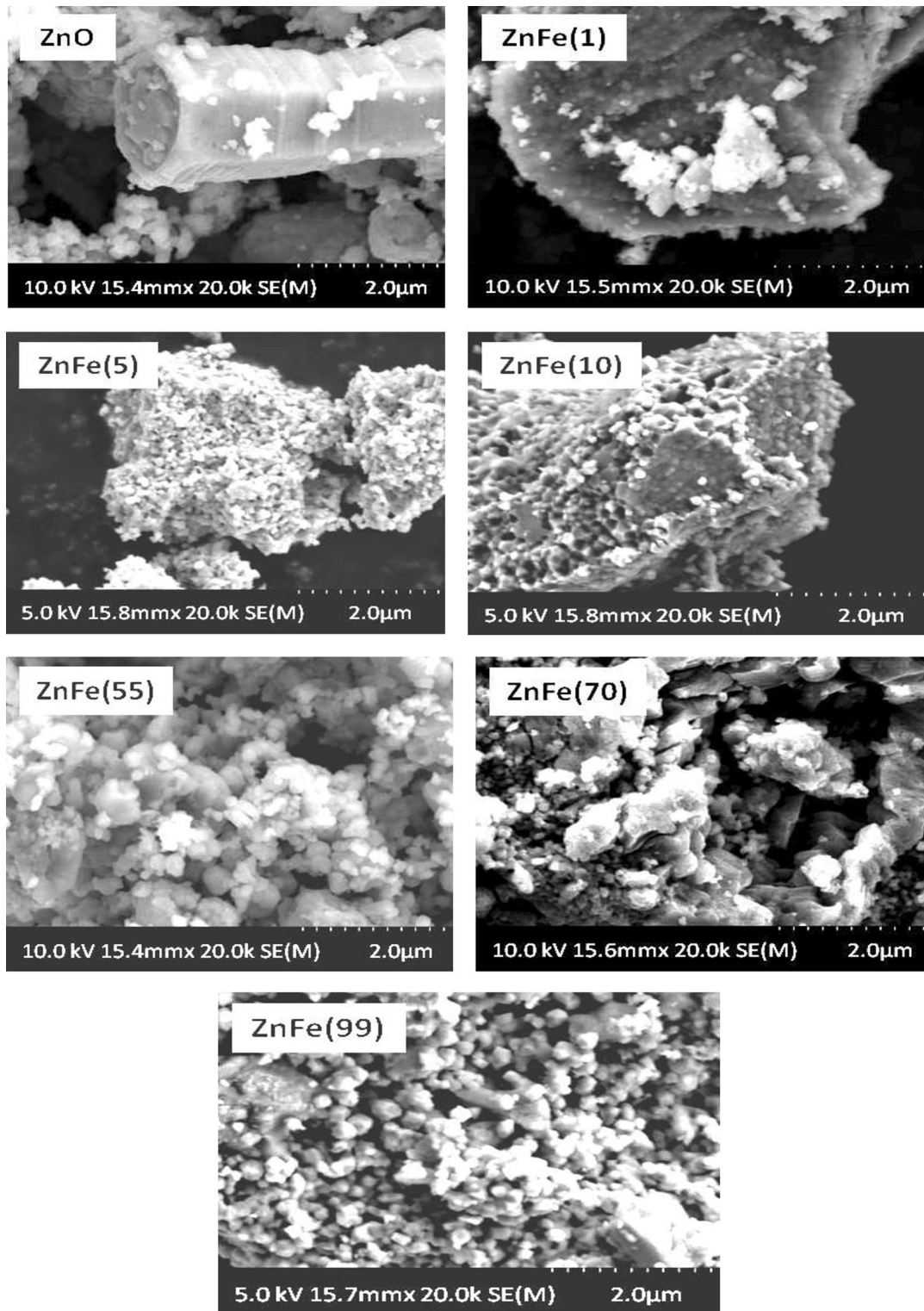
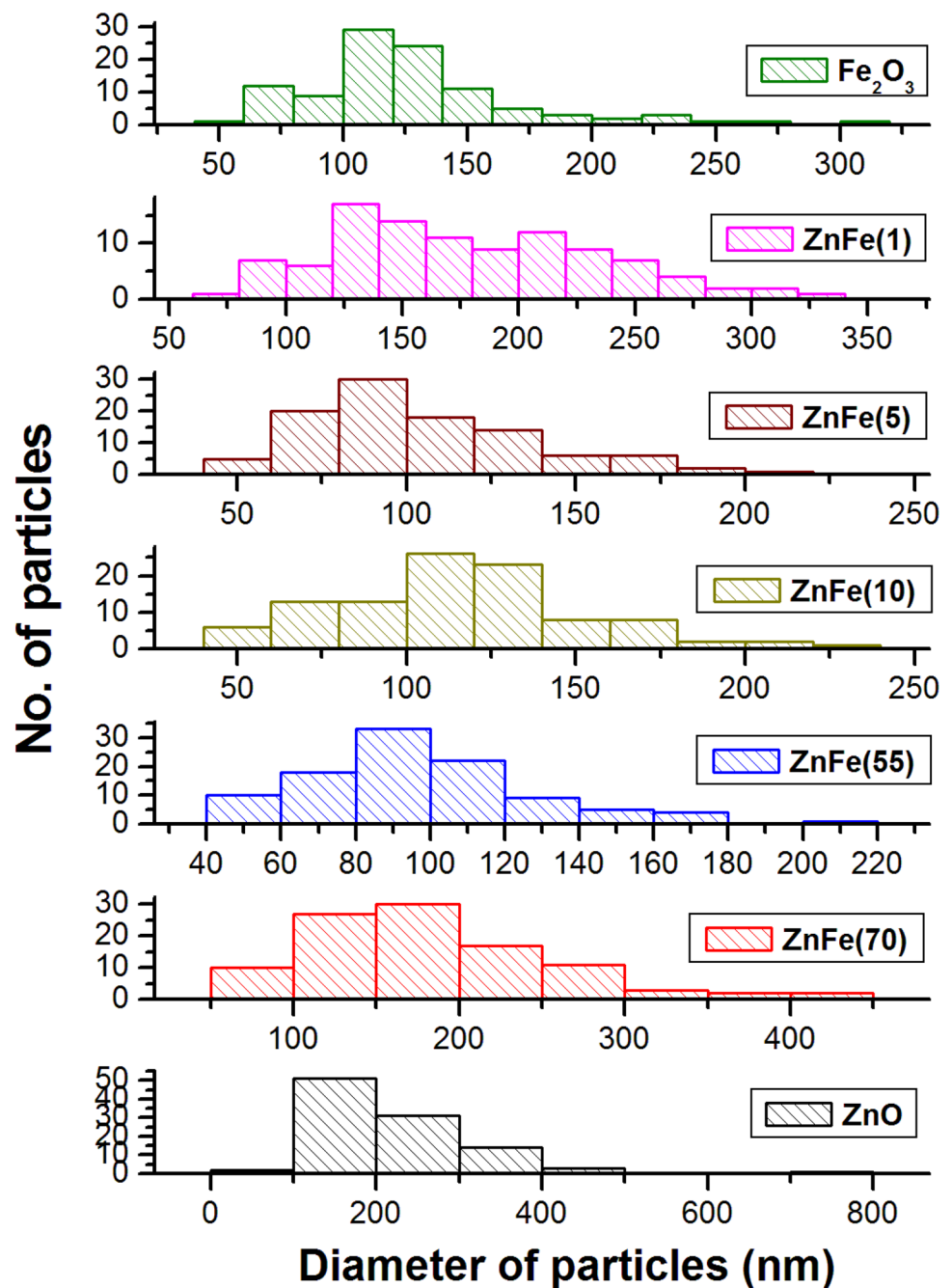


Fig. 3 SEM images of samples

Fig. 4 Particle size distribution in samples, estimated from SEM analysis



3.4 Mössbauer spectroscopic study

The Mössbauer spectra of samples (Fig. 8) show the local magnetic environment around Fe sites and indicates about the oxidation state of the Fe. Table 3 gives the hyperfine field values (H_{hf}), isomer shift (δ), quadrupole splitting (ΔE_Q), outer line width (Γ) and relative areas (R_A) in percentage of doublet (paramagnetic) and sextet (Zeeman splitting pattern) sites of Fe³⁺ ions. Each spectrum shows a paramagnetic doublet with isomer shift (δ) ranging 0.340–0.347 mm s⁻¹ and quadrupole splitting

(ΔE_Q) 0.36–0.41 mm s⁻¹, indicating trivalent nature with high spin of the Fe atoms in samples. As reported earlier [38] a similar doublet ($\delta = 0.56$ mm s⁻¹) was observed for nanocrystalline 10% Fe-doped ZnO powder. Samples with $\leq 80\%$ Fe content showed a magnetic sextet with isomer shift (δ) ranging 0.354–0.372 mm s⁻¹ and magnetic hyperfine field (H_{hf}) 52.0–52.2 T, indicating trivalent nature of the Fe atom in samples. Values of isomer shift (δ) and quadrupole splitting (ΔE_Q) for the doublet and sextet show that Fe is in tetrahedral site [45, 46]. No signature of Fe²⁺ has been found in spectrum of any sample. Had Fe been present

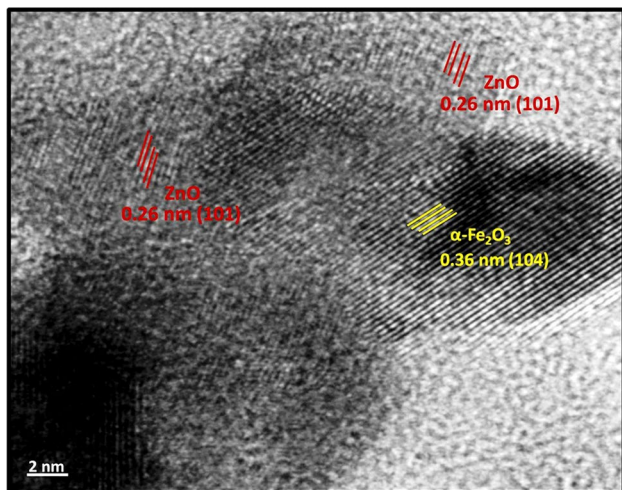


Fig. 5 TEM image of sample ZnFe(70)

in the substitutional site in a defect-free host crystal, its valence state should have been +2. However, Mössbauer results confirm the presence of uncoupled Fe³⁺ within the sample giving rise to the associated paramagnetic behavior [47]. Figure 9 shows the relative area ratio (%) of the two phases; paramagnetic doublet and magnetic sextet for samples. It is clear that up to 70% Fe content only one paramagnetic doublet exist, whereas at higher concentrations a magnetic sextet also coexists. Relative area of doublet decreases and sextet area increases at Fe content above 70%. The variation in Quadrupole splitting

of superparamagnetic doublet and magnetic sextet in samples with increasing Fe content (*x*) is shown in Fig. 10. There occurred reduction in the quadrupole splitting in doublet (Fig. 9 inset a), as the Fe concentration is increased which suggests that the asymmetry decreases at Fe sites. The ΔE_Q values are found to be different for two Fe sites (doublet and sextet). Since, ΔE_Q occurs due to an interaction between nuclear quadruple moment and electric field gradient, produced by surrounding ions, the different values of ΔE_Q for the two sites suggest different local environments. The higher value of ΔE_Q for the doublet site as compared to that for the other site (sextet) indicates the presence of a relatively larger crystal field gradient at the doublet site. Also, quadrupole splitting of sextet decreases with increasing Fe content shown in Fig. 9 (inset b).

3.5 XPS analysis

Sample ZnFe(70) was subjected to XPS analysis (Fig. 11). C 1s peak at 284.5 eV was used as reference for calibration of binding energy. The core spectrum of Zn 2p indicates +2 oxidation state of Zn, as evident from Zn 2p_{3/2} and Zn 2p_{1/2} peaks at binding energy 1020 and 1042 eV, respectively. Further, +3 oxidation state of Fe is also indicated from Fe 2p_{3/2} and Fe 2p_{1/2} peaks at binding energy 711 and 723 eV, respectively. Few satellite peaks of Fe are also seen in the observed pattern at binding energy 781, 847 and 897 eV. Prominently seen peak at binding energy 529.5 eV corresponds to O 1s, largely attributable to surface bridging oxygen.

Fig. 6 Diffuse reflectance UV-Visible spectra of samples

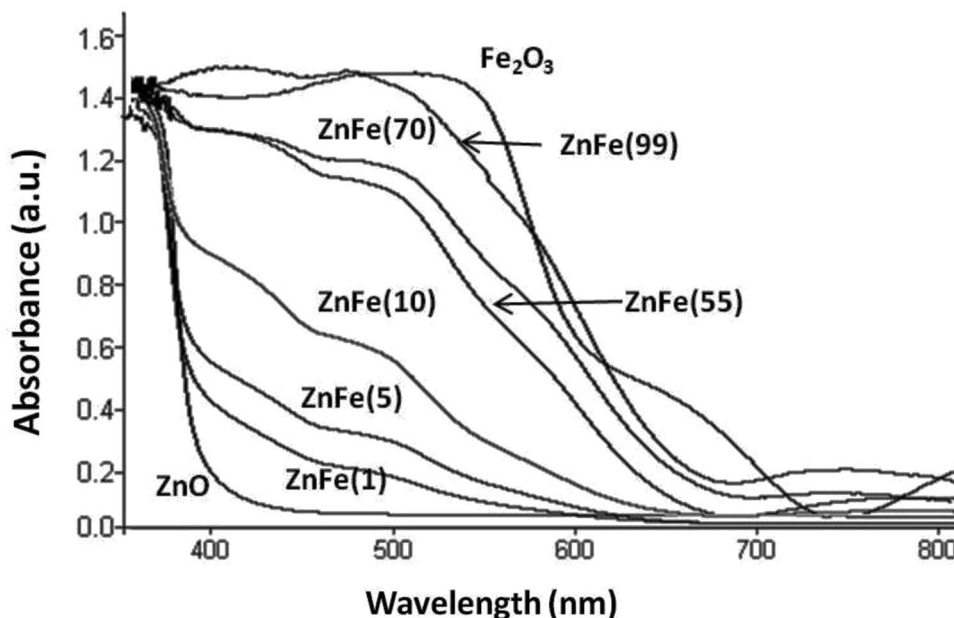
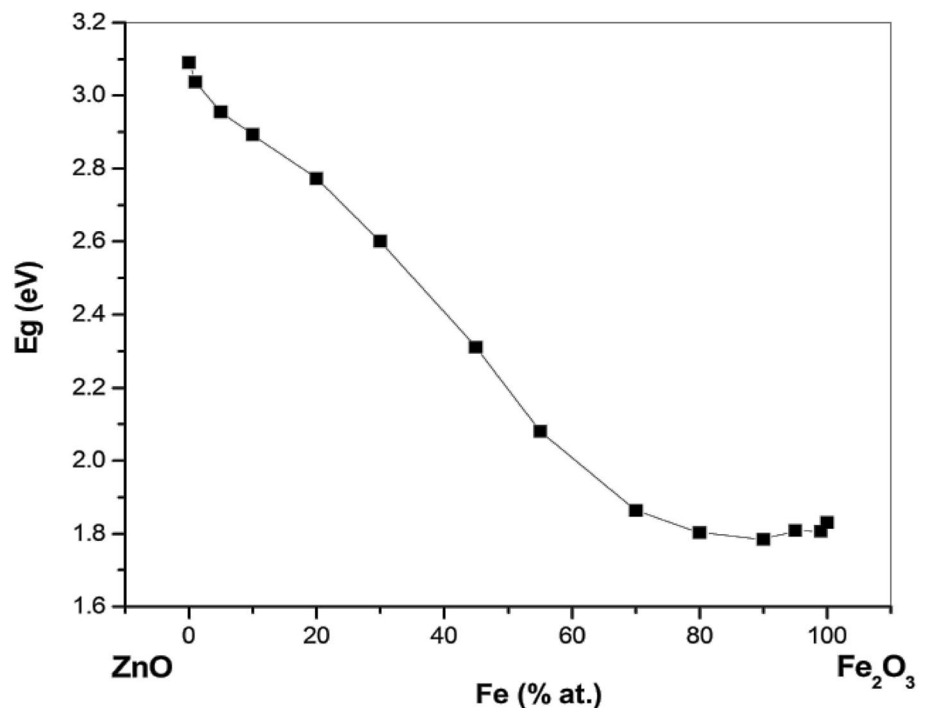


Fig. 7 Band gap energy (E_g) of samples as estimated from diffuse reflectance UV–Visible spectral analysis



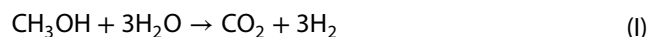
3.6 Photoelectrochemical studies

Photoelectrochemical cell current (J) increased with rise in external bias/potential (V) and upon illumination. The nature of J – V curves confirmed n-type behaviour of samples. In earlier works by authors on ZnO [48, 49] the dark current was found almost zero suggesting a well formed depletion layer. However, in this study the dark current in the range 0.2 – 0.3 mA cm^{-2} (at zero bias) was seen with all the samples, which indicates part-permeability of the depletion layer and/or creation of surface states. The rise in current under illumination has been quantified as photocurrent (J_{PH}) and its variation with applied bias is presented in Fig. 12. Two samples, ZnFe(10) and ZnFe(55) that did not yield any significant photocurrent, have been omitted from the presentation. Photocurrent density (J_{PH}) varied with samples' composition and applied bias (Table 5). Sample ZnFe(70) yielded maximum photocurrent density 3.65 mA cm^{-2} at 700 mV bias, marking a gain in photocurrent of nearly 100 and 600% against pure α - Fe_2O_3 and ZnO, respectively, under similar conditions of measurement. The effect may be attributed to almost a linear fall noticed in the bandgap energy as Zn/Fe atomic ratio decreases (Fig. 3), with ZnFe(70) exhibiting lowest bandgap of 1.8 eV. Going further, from sample ZnFe(70) to Fe_2O_3 , no significant change occurs to the band gap energy. Still, the increasing dominance of α - Fe_2O_3 phase in samples, which is known to be a high resistance material [50], appears to weaken the PEC response by limiting the charge transport kinetics. As Fe content increases, the

spinel phase diminishes with dominant commencement of Fe_2O_3 phase. The ZnFe(70) sample, however, consists of both the spinel and Fe_2O_3 phases. The computed ABPE of the sample ZnFe(70) was 2.14% as against 1.05 and 0.34% for pure α - Fe_2O_3 and pure ZnO samples, respectively.

3.7 Photocatalytic studies

Figure 13 depicts the observed photocatalytic hydrogen generation over the samples from water–methanol solution under UV–visible illumination. Methanol served as hole scavenger, controlled addition of which is known to enhance electron–hole separation [18]. Nonetheless, part consumption of methanol through oxidation also occurs as,



Under the optimized conditions in presence of methanol, nearly 1/3rd of the total hydrogen evolved comes from the dissociation of water [8]. As can be seen from Fig. 10 the sample ZnFe(99) exhibited maximum hydrogen production (123 $\mu\text{ moles h}^{-1} \text{ g}^{-1}$) and the yield is almost double to the value recorded with pure α - Fe_2O_3 (68 $\mu\text{ moles h}^{-1} \text{ g}^{-1}$) and triple to pure ZnO (43 $\mu\text{ moles h}^{-1} \text{ g}^{-1}$). The sample ZnFe(1) also showed increased hydrogen production (116 $\mu\text{ moles h}^{-1} \text{ g}^{-1}$). All other samples with intermediate concentrations of Fe were found to be less responsive for PC hydrogen generation. The secondary phase (ZnFe_2O_4) evolved dominantly in samples ZnFe(10) and ZnFe(55) also seems not to support PC splitting of water. Table 4

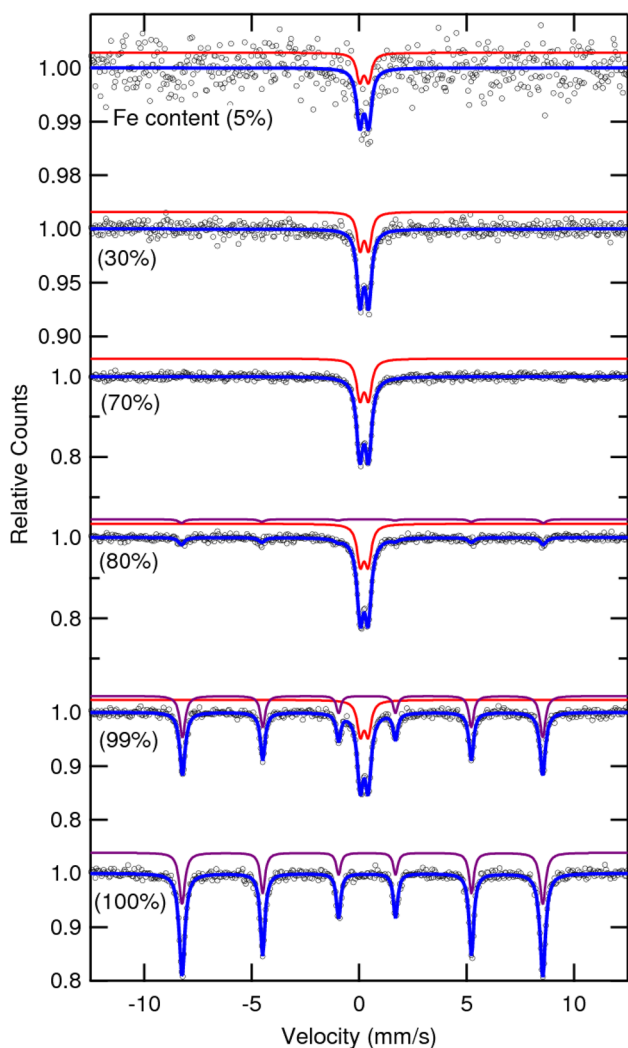


Fig. 8 Mössbauer spectra of samples with different Fe content. Blue line is the experimental data (shown as open circles) fitted line. Red and purple color lines belong, respectively, to doublet and sextet (Zeeman splitting) components

presents the observed yield of H₂ and estimated Apparent Quantum Efficiency (AQE) of the systems investigated. Experiments conducted in the absence of irradiation and/or photocatalyst resulted in insignificant evolution of H₂. Further, in photocatalytic experiments, amount of H₂ evolved increased almost linearly with increase in irradiation time with all samples (Fig. 13).

A comparison of the PEC/PC performance of the best samples drawn from the present study against results observed in few earlier works (Table 5) suggests significant improvement in the performance. The basic problem with most high efficiency systems reported in literature for PEC/PC splitting of water that has impeded their commercial application so far is often non-repetitive and exorbitantly expensive and complex material-processing involved. To that extent, nanocomposites investigated in the present study are definitely low-cost and are evolved from abundantly available semiconductors.

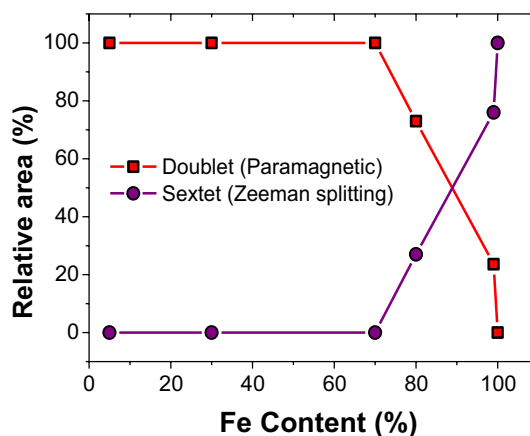


Fig. 9 Variation in relative area ratio of paramagnetic doublet and magnetic sextet (Zeeman splitting pattern) in samples with increasing Fe content

Table 3 The hyperfine field values (H_{hf}), isomer shift (δ), quadrupole splitting (ΔE_Q), outer line width (Γ) and relative area (R_A) of doublet (super-paramagnetic) and sextet (magnetic) sites of Fe³⁺ ions in samples (derived from Mössbauer spectra, recorded at room temperature)

Sample abbreviate	Metal concentration (at.%) in samples Zn Fe	Iron sites	^a (mm s^{-1})	ΔE_Q (mm s^{-1})	H_{hf} (Tesla)	Γ (mm s^{-1})	R_A (%)
ZnFe(5)	95 5	Doublet	0.340	0.410	–	0.347	100
ZnFe(30) ^b	70 30	Doublet	0.347	0.399	–	0.329	100
ZnFe(70)	30 70	Doublet	0.341	0.402	–	0.360	100
ZnFe(80) ^b	20 80	Doublet	0.343	0.364	–	0.358	73
		Sextet	0.354	–0.191	52.21	0.346	27
ZnFe(99)	1 99	Doublet	0.345	0.365	–	0.338	24
		Sextet	0.372	–0.207	51.97	0.240	76
Fe ₂ O ₃	– 100	Sextet	0.366	–0.217	52.04	0.241	100

^aIsomer shift results are relative to Fe metal foil

^bAdditional samples prepared for Mössbauer analysis

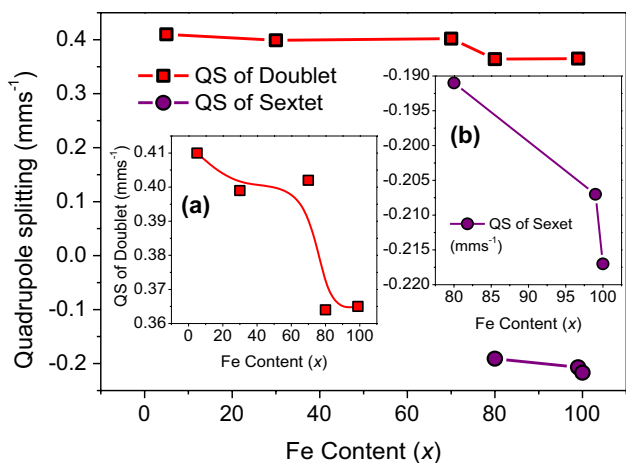


Fig. 10 Variation in quadrupole splitting of superparamagnetic doublet and magnetic sextet in samples with increasing Fe content (x)

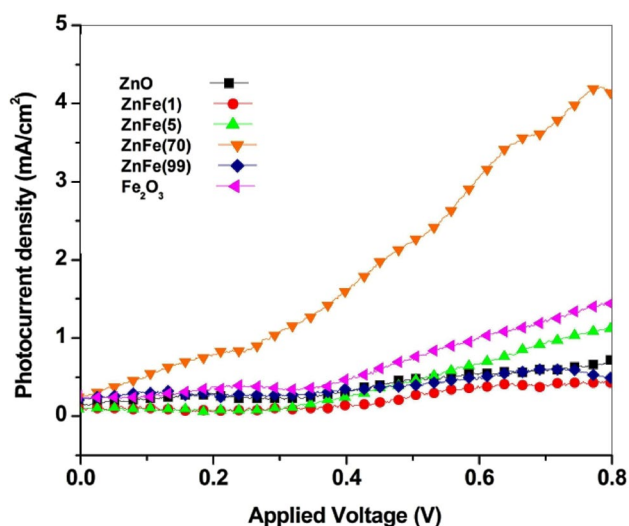


Fig. 12 PEC photocurrent observed at varied applied voltage (vs. SCE)

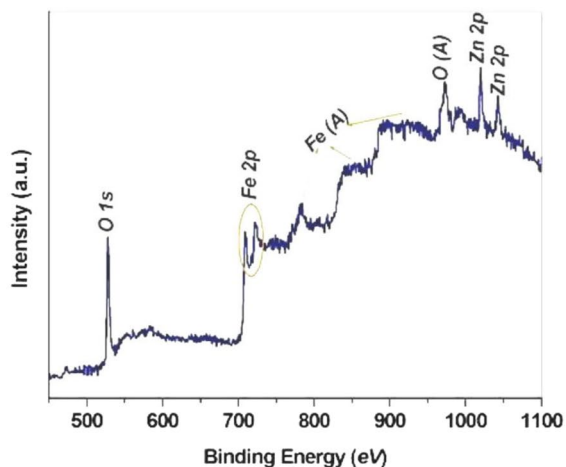
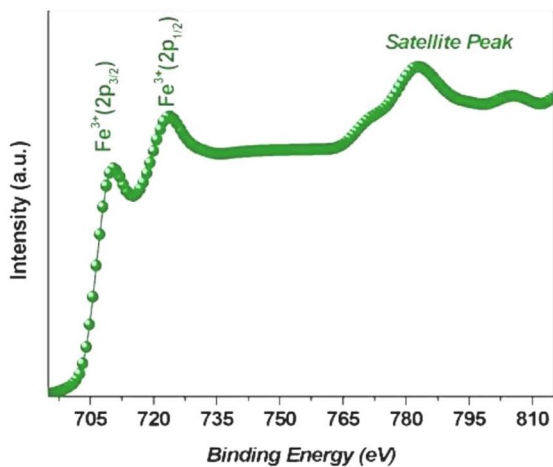
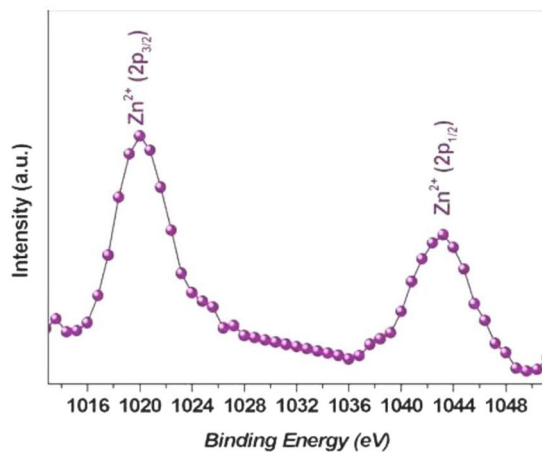
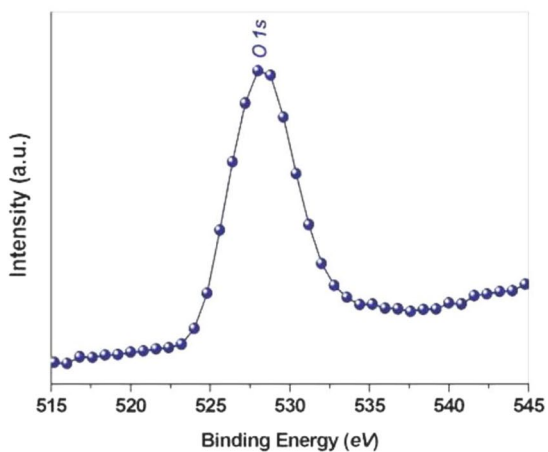


Fig. 11 XPS pattern of sample ZnFe(70)

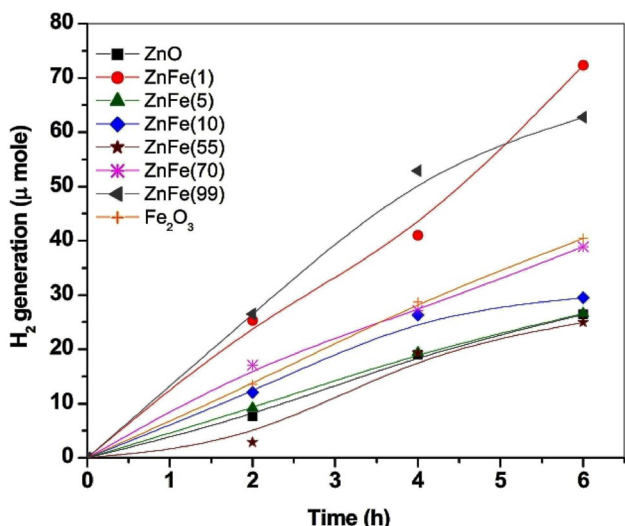


Fig. 13 Photocatalytic H₂ generation observed at different times under the reaction conditions: 0.1 g photocatalyst, 10 cm³ distilled water, 5 cm³ methanol

4 Conclusions

The present study, thus, leads to the following important conclusions: (1) Evolution of wurtzite ZnO and α-Fe₂O₃ dominantly occur in samples at extreme ends of Zn/Fe atomic ratios. At intermediate concentration ratios the formation of ZnFe₂O₄ spinels occurs. (2) Light absorption threshold frequency shifts downward with decrease in Zn/Fe atomic ratio. However, the absorption appears to be largely due to the cumulative effect of the simultaneous existence of two oxides. (3) Despite the basic phenomenon of photoexcitation, electron–hole pair separation and their participation in redox processes pertaining to splitting of water, being the same, the conditions for optimized evolution of hydrogen via PEC and PC routes are different. (4) Compared to pure α-Fe₂O₃, the sample ZnFe(70) with a possibly controlled presence of ZnFe₂O₄ appeared more effective for PEC splitting of water. The effect is attributable to increase in optical absorption along with fall in electrical resistivity. (5) For PC hydrogen generation, single

Table 4 A comparative performance of samples in PEC and PC splitting of water

Sample abbreviate	Nominal composition (Zn _{1-x} Fe _x O _y)	PEC performance		PC performance	
		J _{PH} ^a (mA cm ⁻²)	ABPE (%)	H ₂ yield ^b (μ moles h ⁻¹ g ⁻¹)	AQE (%)
ZnO	ZnO	0.59	0.34	43	3.52
ZnFe(1)	Zn _{0.99} Fe _{0.01} O	0.44	0.25	116	9.50
ZnFe(5)	Zn _{0.95} Fe _{0.05} O	0.97	0.57	52	4.26
ZnFe(10)	Zn _{0.9} Fe _{0.1} O	0.75	0.44	58	4.75
ZnFe(55)	Zn _{0.45} Fe _{0.55} O	0.10	0.05	35	2.87
ZnFe(70)	Zn _{0.30} Fe _{0.70} O	3.65	2.14	73	5.98
ZnFe(99)	Zn _{0.01} Fe _{0.99} O	1.23	0.72	123	10.08
Fe ₂ O ₃	Fe ₂ O ₃	1.50	0.88	69	5.65

^aValues recorded at 700 mV bias versus SCE

^bTime average value obtained for 6 h run

Table 5 A comparison of PEC/PC performance of samples prepared in the present study vis-à-vis the values reported earlier

Semiconductor/material system used	PEC performance			PC performance			References
	Electrolyte	Applied bias (mV)	J _{PH} (mA cm ⁻²)	Co-catalyst/dopant	Reaction solution	H ₂ yield (μ mole h ⁻¹)	
Sample ZnFe(70)	NaOH (pH 12)	700 ^a	3.65	–	–	–	Present study
Sample ZnFe(99)	–	–	–	–	CH ₃ OH + H ₂ O	12.3	Present study
ZnGeON	–	–	–	Rh _{2-x} Cr _x O ₃	CH ₃ OH + H ₂ O	11.1	[51]
K ₄ Nb ₆ O ₁₇	–	–	–	–	H ₂ O	8.1	[52]
Pt/SrTiO ₃ : Rh, WO ₃	–	–	–	–	2 mM FeCl ₃	7.8	[53]
Fe-doped BaTiO ₃	NaOH (0.1 M)	500 ^a	2.55	–	–	–	[27]
C-doped In ₂ O ₃	KOH (1 M)	800 ^b	1.00	–	–	–	[54]
Cu ₂ O	Na ₂ SO ₄ (0.5 M)	300 ^b	0.14	–	–	–	[55]

^aVersus saturated calomel electrode

^bVersus silver–silver chloride electrode

phase doped ZnO or α -Fe₂O₃ emerge as better systems. A mild doping (up to 5 at.%) by the alternate cation resulted in improved PC performance.

Acknowledgements Financial assistance from Govt. of India through UGC (F. No. 194-1/2009 (IC); July 2015) in the form of R & D projects sanctioned to RS is gratefully acknowledged. Authors are also thankful to Dr. Sadhana Railu, EMD, NEERI, Nagpur, India for DR-UV analyses of samples.

Compliance with ethical standards

Conflict of interest On behalf of all authors, the corresponding author states that there is no conflict of interest.

References

- Abbasi T, Abbas SA (2011) Renewable hydrogen: prospects and challenges. *Renew Sustain Energy Rev* 15:3034–3040
- Agrawal R, Offutt M, Ramage MP (2005) Hydrogen economy—an opportunity for chemical engineers. *AIChE J* 51:1582–1589
- Maeda K, Teramura K, Saito N et al (2006) Overall water splitting using nitride photocatalysts. *Pure Appl Chem* 78:2267–2276
- Bak T, Nowotny J, Rekas M et al (2002) Photo-electrochemical hydrogen generation from water using solar energy materials-related aspects. *Int J Hydrog Energy* 27:991–1022
- Kudo A, Miseki Y (2009) Heterogeneous photocatalyst materials for water splitting. *Chem Soc Rev* 38:253–278
- Fujishima A, Honda K (1972) Electrochemical photolysis of water at a semiconductor electrode. *Nature* 238:37–38
- Kitano M, Hara M (2010) Heterogeneous photocatalytic cleavage of water. *J Mater Chem* 20:627–641
- Ni M, Leung MKH, Leung DYC et al (2007) A review and recent developments in photocatalytic water-splitting using TiO₂ for hydrogen production. *Renew Sustain Energy Rev* 11:401–425
- Park H, Choi W, Hoffmann MR (2008) Effects of the preparation method of the ternary CdS/TiO₂/Pt hybrid photocatalysts on visible light-induced hydrogen production. *J Mater Chem* 18:2379–2385
- Yooa SJ, Yunb SU, Sungb YE et al (2010) Tungsten oxide bilayer electrodes for photoelectrochemical cells. *J Power Sour* 195:5422–5425
- Solanki A, Shrivastava J, Upadhyay S et al (2011) Irradiation-induced modifications and PEC response: a case study of SrTiO₃ thin films irradiated by 120 MeV Ag⁹⁺ ions. *Int J Hydrog Energy* 36:5236–5245
- Wang A, Yang H, Song T, Sun Q, Liu H, Wang T, Zeng H (2017) Plasmon mediated Fe–O in an octahedral site of cuprospinel by Cc NPs for photocatalytic hydrogen evolution. *Nanoscale* 9:15760–15765
- Song T, Huo J, Liao T, Zeng J, Qin J, Zeng H (2016) Fullerene [C₆₀] modified. Cr_{2–x}Fe_xO₃ nanocomposites for enhanced photocatalytic activity under visible light irradiation. *Chem Eng J* 287:359–366
- Zeng J, Song T, Lv M, Wang T, Qin J, Zeng H (2016) Plasmonic photocatalyst Au/g–C₃N₄/NiFe₂O₄ nanocomposites for enhanced visible-light-driven photocatalytic hydrogen evolution. *RSC Adv* 6:54964
- Song T, Zhang P, Zeng J, Wang T, Alia A, Zeng H (2017) Boosting the photocatalytic H₂ evolution activity of α -Fe₂O₃ polymorphs (α -, γ - and β -Fe₂O₃) by fullerene (C₆₀)-modification and dye-sensitization under visible light irradiation. *RSC Adv* 7:29184
- Campet G, Deshayes A, Frison JC et al (1998) Applications of nanoscale materials in the fields of electrochemistry and photoelectrochemistry. *Acta Pass Electrode Compd* 1:123–146
- Zhu J, Zach M (2009) Nanostructured materials for photocatalytic hydrogen production. *Curr Opin Colloid Interface Sci* 14:260–269
- Chen Z, Jaramillo TF, Deutsch TG et al (2010) Accelerating materials development for PEC hydrogen production: standards for methods, definitions and reporting protocols. *J Mater Res* 25:3–16
- Huo J, Fang L, Lei Y, Zeng G, Zeng H (2014) Facile preparation of yttrium and aluminium co-doped ZnO via a sol–gel route for photocatalytic hydrogen production. *J Mater Chem A* 2:11040
- Liu H, Zhao K, Wang T, Deng J, Zeng H (2015) Facile preparation of cerium (Ce) and antimony (Sb) co-doped SnO₂ for hydrogen production in lactic acid solution. *Mater Sci Semicond Process* 40:670–675
- Alexander BD, Kulesza PJ, Rutkowska I et al (2008) Metal oxide photoanodes for solar hydrogen production. *J Mater Chem* 18:2298–2303
- Kudo A (2003) Photocatalyst materials for water splitting. *Catal Surv Asia* 1:31–38
- Li Y, Yu H, Song W et al (2011) A novel photoelectrochemical cell with self-organized TiO₂ nanotubes as photoanodes for hydrogen generation. *Int J Hydrog Energy* 36:14374–14380
- Sreethawong T, Junbua C, Chavadej S et al (2009) Photocatalytic H₂ production from water splitting under visible light irradiation using eosin Y-sensitized mesoporous-assembled Pt/TiO₂ nanocrystal photocatalyst. *J Power Sour* 190:513–524
- Zhang J, Bang JH, Tang C et al (2010) Tailored TiO₂–SrTiO₃ heterostructure nanotube arrays for improved photoelectrochemical performance. *J Am Chem Soc* 4:387–395
- Drake C, Seal S (2007) Band gap energy modifications observed in trivalent in substituted nanocrystalline SnO₂. *App Phys Lett* 90:233117–233122
- Upadhyay S, Shrivastava J, Solanki A (2011) Enhanced photoelectrochemical response of BaTiO₃ with Fe doping: experiments and first principle analysis. *J Phys Chem C* 115:24373–24380
- Yuan G, Zhao H, Hasanali ZS et al (2009) Synthesis and photoelectrochemical study of vertically aligned silicon nanowire arrays. *Angew Chem Int Ed* 48:9680–9684
- Chandra S, Khare N, Upadhyaya HM (1988) Photoelectrochemical solar cells using electrodeposited GaAs and AlSb semiconductor films. *Bull Mater Sci* 10:323–332
- Blackburn JL, Selmarten DC, Ellingson RJ et al (2005) Electron and hole transfer from indium phosphide quantum dots. *J Phys Chem B* 109:2625–2631
- Valenzuela MA, Bosch P, Becerrill JJ et al (2002) Preparation, characterization and photocatalytic activity of ZnO, Fe₂O₃ and ZnFe₂O₄. *J Photochem Photobio A Chem* 148:177–182
- Ahn KS, Shet SR, Deutsch T et al (2008) Enhancement of photoelectrochemical response by aligned nanorods in ZnO thin films. *J Power Sour* 176:387–392
- Hahn NT, Ye H, Flaherty DW et al (2010) Reactive ballistic deposition of α -Fe₂O₃ thin films for photoelectrochemical water oxidation. *J Am Chem Soc* 4:1977–1986
- Han J, Shen M, Cao W (2003) Hopping conduction in Mn-doped ZnO. *Appl Phys Lett* 82:67–69
- Sharma V, Kumar P, Singh N et al (2012) Photoelectrochemical water splitting with nanocrystalline Zn_{1–x}Ru_xO thin films. *Int J Hydrog Energy* 37:12138–12149
- Sharma V, Kumar P, Shrivastava J et al (2011) Synthesis and characterization of nanocrystalline Zn_{1–x}M_xO (M = Ni, Cr) thin films for efficient photoelectrochemical splitting of water under UV irradiation. *Int J Hydrog Energy* 36:4280–4290

37. Sharma S, Pai MR, Kaur G et al (2018) Efficient hydrogen generation on CuO core/Ag–TiO₂ shell nano-hetero structures by photocatalytic splitting of water. *Renew Energy*. <https://doi.org/10.1016/j.renene.2018.09.091>
38. Hernandez A, Maya L, Sanchezmora E et al (2007) Sol–gel synthesis and photocatalytic activity of mixed oxide ZnO–Fe₂O₃. *J Sol Gel Sci Technol* 12:71–78
39. Kathirvel P, Manoharan D, Mohan SM et al (2009) Spectral investigations of chemical bath deposited zinc oxide thin films— ammonia gas sensor. *J Optoelectron Biomed Mater* 1:25–33
40. Pai MR, Majeed J, Banerjee AM et al (2012) Role of Nd³⁺ ions in modifying band structure and photocatalytic properties of substituted indium titanates, In_{2(1-x)}Nd_{2x}TiO₅ oxides. *J Phys Chem C* 116:1458–1462
41. Guskos N, Kiewicz GZ, Typek J et al (2010) Magnetic resonance study of ZnO–Fe₂O₃–ZnFe₂O₄ system. *Rev Adv Mater Sci* 23:224–228
42. Johnston DC (1976) Superconducting and normal state properties of Li_{1+x}Ti_{2-x}O₄ spinel compounds: preparation, crystallography, superconducting properties, electrical resistivity, dielectric behavior, magnetic susceptibility. *J Low Temp Phys* 25:145–151
43. Borse PH, Jang JS, Hong SJ et al (2009) Photocatalytic hydrogen generation from water-methanol mixtures using nanocrystalline ZnFe₂O₄ under visible light irradiation. *J Korean Phys Soc* 55:1472–1477
44. Sibera D, Jedrzejewski R, Mizeracki J et al (2009) Synthesis and characterization of ZnO doped with Fe₂O₃—hydrothermal synthesis and calcination process. *Acta Physica Polonica* 116:S133–S135
45. Karmakar D, Mandal SK, Nath TK (2007) Ferromagnetism in Fe-doped ZnO nanocrystals: experimental and theoretical investigations. *Phys Rev B* 75:144401–144414
46. Chinnasamy CN (2000) Magnetic properties of nanostructured ferrimagnetic zinc ferrite. *J Phys Condens Mater* 12:7795–7800
47. Roy A, Kumar S, Banerjee D et al (2000) Mossbauer studies on titanium substituted molybdenum ferrite. *Solid State Commun* 114:143–147
48. Gupta M, Shrivastava J, Sharma V et al (2009) Enhanced photoelectrochemical activity of 120 MeV Ag⁹⁺ irradiated nanostructured thin films of ZnO for solar-hydrogen generation via splitting of water. *Adv Mater Res* 67:95–102
49. Sharma V, Kumar P, Shrivastava J et al (2011) Vertically aligned nanocrystalline Cu–ZnO thin films for photoelectrochemical splitting of water. *J Mater Sci* 46:3792–3801
50. Tai YW, Yang CC, Yang MH et al (2011) Preparation and characterization of p-type Fe₂O₃ pellets from Mg doping in pure oxygen atmosphere at high temperatures. *J Taiwan Inst Chem Eng* 42:669–673
51. Tessier F, Pascal M, Yungi L et al (2009) Zinc germanium oxynitride: influence of the preparation method on the photocatalytic properties for overall water splitting. *J Phys Chem C* 113:8526–8531
52. Matsuoka M, Kitano M, Takeuchi M et al (2007) Photocatalysis for new energy production: recent advances in photocatalytic water splitting reactions for hydrogen production. *Catal Today* 122:51–61
53. Kato H, Hori M, Kanta R et al (2004) Construction of Z-scheme type heterogeneous photocatalysis systems for water splitting into H₂ and O₂ under visible light irradiation. *Chem Lett* 33:1348–1349
54. Yanping SY, Murphy CJ, Reyes-Gil KR et al (2008) Carbon-doped In₂O₃ films for photoelectrochemical hydrogen production. *Int J Hydrog Energy* 33:5967–5974
55. Meng LR, Min CY, Wei WP (2010) Effect of annealing on the electrodeposited Cu₂O films for photoelectrochemical hydrogen generation. *Thin Solid Films* 518:7191–7195

Publisher's Note Springer Nature remains neutral with regard to jurisdictional claims in published maps and institutional affiliations.